Infrared confocal imaging for inspection of flaws in yttria-stabilized tetragonal zirconia polycrystal (Y-TZP)

Matysiak, Mateusz; Parry, Jonathan P.; Albri, Frank; Crowder, J. Graham; Jones, Nick; Jonas, Kevyn; Weston, Nick; Hand, Duncan Paul; Shephard, Jonathan D

Published in:
Measurement Science and Technology

DOI:
10.1088/0957-0233/22/12/125502

Publication date:
2011

Infrared confocal imaging for inspection of flaws in Yttria-Stabilised Tetragonal Zirconia Polycrystal (Y-TZP)

Mateusz Matysiak[†], Jonathan P. Parry[†], Frank Albri[†], J. Graham Crowder[†], Nick Jones[‡], Kevyn Jonas[‡], Nick Weston[‡], Duncan P. Hand[†] and Jonathan D. Shephard[†]

†School of Engineering and Physical Sciences, Heriot-Watt University, Edinburgh, EH14 4AS, UK

[‡]Dental Products Division, Renishaw plc, New Mills, Wotton-under-Edge, Gloucestershire, GL12 8JR, UK

email: mm355@hw.ac.uk

Abstract

Custom made medical Yttria-Stabilized Tetragonal Zirconia Polycrystal (Y-TZP) components require a high standard of machining and inspection techniques to ensure high reliability of the manufactured parts. Due to heat generated during machining processes, which in turn can cause cracking, the strength of Y-TZP ceramics can be compromised. Thus, a novel Confocal Mid-Infrared Transmission Imaging (CMIR-TI) technique is introduced in this paper. It provides enhanced imaging capabilities for flaws and cracks introduced into the bulk of the component compared to previously developed imaging techniques. We demonstrate that micrometre scale cracks can be identified in Y-TZP components up to 3.5 mm thick with an imaging resolution of approximately 30 μm, and also show that macro scale flaws can be observed in the volume of Y-TZP ceramics of up to 7 mm thick.

Keywords: non-destructive testing, optical inspection, mid-infrared imaging, zirconia, dental, medical.

1.0. Introduction

There exists an increasing demand for high toughness, high strength materials driven by a wide range of applications where high wear resistance with thermal and mechanical stability is necessary. One such material is the ceramic Yttria-Stabilized Tetragonal Zirconia Polycrystal (Y-TZP), which has been applied in a variety of fields ranging from medical [1-3] and high temperature applications [4, 5] to high mechanical wear environments [6, 7] where its superior strength arising from a transformation toughening mechanism [8, 9] is a favourable property. Additionally, the biocompatibility of Y-TZP makes it particularly useful for medical applications [10-12].

Conventionally Y-TZP is machined in a hard state using mechanical grinding and sandblasting techniques [13, 14]. Additionally, laser machining techniques suitable for Y-TZP have been developed by our group [15-18] to increase the machining speed and reduce the cost due to tool wear. A considerable challenge of either mechanical or laser machining exists due to the thermal load introduced during processing of Y-TZP which may lead to material cracking resulting from the high thermal gradients involved [16, 19]. This therefore restricts the overall processing speed, or fabrication time of a particular component, to ensure cracks are kept to minimum.

Figure 1 presents an image of a failed component after laser machining that was not optimized. Naturally, these cracks and flaws reduce the strength, and ultimately the overall lifetime, of the ceramic component. Unfortunately, no matter how careful the processing, there is always a risk of forming cracks. Therefore a component cannot be used unless there is a high certainty that cracking is not an issue. This is particularly important in biomedical applications with the added complication that each component is a unique final part and therefore must be thoroughly inspected before going into service. Consequently, ceramic parts, such as dental replacement crowns and bridges, are inspected manually with a visible light source which is very time consuming and may not detect fine cracks which can lead to in-service failure.

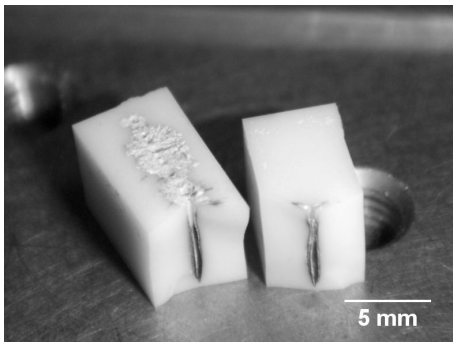

Figure 1. A shattered Y-TZP block after laser machining which was not optimized to reduce cracking.

The aforementioned challenges require the development of a non-destructive means of inspection of Y-TZP ceramics. However, its unique optical properties due to light scattering [20] substantially reduce the applicability of various, optical based, non-destructive techniques. Some attempts to develop inspection techniques for zirconia parts are described in the literature [21-32], but none of these techniques is applicable for crack detection in thick ceramic components. Recently, the Mid-Infrared Transmission Imaging (MIR-TI) technique was presented by our group [33] which significantly increased the thickness of the component which can be examined non-destructively. Infrared radiation transmitted through the specimen allows for macro and micro scale features to be imaged and detected very rapidly. However, the resolution of the MIR-TI is limited due to the pixel size of the infrared camera used. An additional barrier is the significant cost of the camera. In this paper we present the development and quantitative evaluation of a new Confocal Mid-Infrared Transmission Imaging (CMIR-TI) technique to improve the resolution and reduce the cost of the imaging system for inspection of Y-TZP parts. The ultimate aim is to develop a relatively compact and robust inspection system that is viable for integration into modern manufacturing processes as a quality control system for zirconia ceramic components.

2.0. The Confocal Mid-Infrared Transmission Imaging (CMIR-TI) technique

The experimental setup of the CMIR-TI system is presented in Figure 2. The infrared camera used previously for the MIR-TI set-up [33] was replaced with a high detectivity Vigo PVI-2TE-8 infrared detector with a 300µm x 300µm active region.

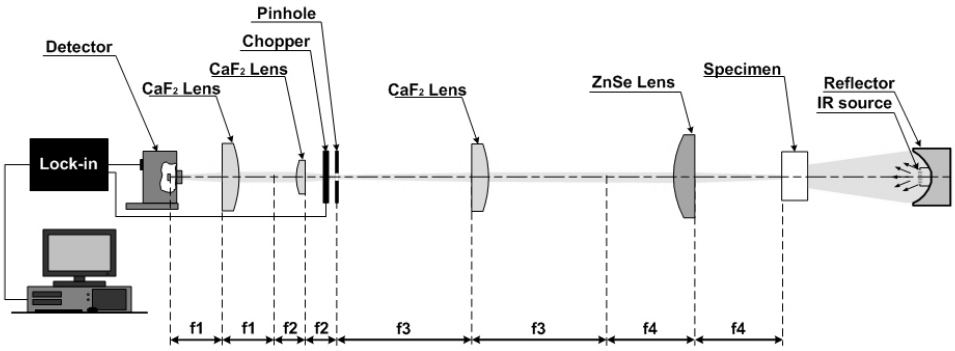

Figure 2. CMIR-TI system setup. Focal lengths of the lenses are as follows: f1 = 40 mm, f2 = 20 mm, f3 = 50 mm, f4 = 38.1 mm. The effective NA of the ZnSe lens measured experimentally is 0.25.

The infrared detector used in the experiments is a mesa structure $Hg_{1-x}Cd_xTe$ photodiode with a response time below 7 ns. The detector is cooled with a thermoelectric cooler (TEC). The chopped AC signal captured by the detector is amplified by the integrated, custom bandwidth (200 Hz to 10 kHz), preamplifier which ensures stable operation and high signal-to-noise ratio (SNR) of the whole system. The chopper and the detector were connected to the lock-in amplifier (Scitec Instruments

Model 420) to enhance signal stability and to reduce any external noise from various heat sources in the laboratory. A 50 μm pinhole (Thorlabs P50C) size was chosen to compare the results with the MIR-TI technique [33] which uses a 50 μm pixel size infrared camera sensor. Another motivation for the choice of a 50 μm pinhole was the limited amount of light reaching the infrared detector. Further reduction of the pinhole size to 25 μm would result a factor of four reduction in signal level which in this particular setup would result in too low SNR. Due to the geometric size difference between the active area of the detector and the pinhole size a 4f lens system images the pinhole onto the detector (Figure 2). This consisted of two CaF_2 lenses (1" and 0.5" diameter lenses) providing a ×2 magnification. Another 4f lens system at the sample side (1" CaF_2 and 1.5" ZnSe diameter lenses) with a magnification of 1.31 was used to image the light transmitted through the sample onto the pinhole.

A broadband 11 Watt infrared source (IR-12K) supplied by Scitec Instruments Ltd [33] was used as the IR light source. This was mounted in a polished aluminium elliptical reflector (Scitec MC-233) to focus the infrared radiation onto the sample.

The sample was mounted on three Standa 8MT173-30DCE (DC) motorized translation stages with 30 mm travel to provide xyz movement of the sample during the scanning process. The resolution of the stages was 100 nm, smallest step size was 140 nm and the bi-directional repeatability 400 nm. The maximum velocity of the stages was 160 μm/s and scanning was controlled via a Labview programme. Figure 3 represents the stages and the scanning sequence chosen for CMIR-TI system. The raster scanning technique in this instance allows not only for fast imaging of the xy planes without the z position error but it also reduces the wear of y and z stages carrying more weight. This xy plane scanning method is one of the main advantages of confocal imaging technique. It allows for slicing of the sample volume, thus imaging the whole sample plane-by-plane. It should be noted that each of the images produced by the CMIR-TI technique and presented in this work represents an image of a single xy plane acquired during the scanning.

Since the pinhole used is 50 μm diameter; initial measurements were performed using 50 μm steps in the x and y axes. Measurements were also repeated with smaller x, y step sizes of 25 and 10 μm to determine whether any improvements in the produced images could be obtained with an increased number of data points acquired. The z stage step size was chosen to be 150 μm, based on the Depth of Field (DOF) parameter calculated from Equation 1 to be 130 μm [33].

$$DOF = \frac{\lambda_0 \cdot \sqrt{n^2 - (NA)^2}}{(NA)^2}, \qquad \text{(Equation 1)}$$

where λ is the wavelength of the illuminating light, n is the refractive index of the medium (air n = 1) between the sample and the objective front lens element and NA is the effective numerical aperture. This was measured by introducing a variable aperture in front of the lens at the sample side. The aperture was positioned next to the optical surface of the lens on the optical axis of the CMIR-TI system. The aperture was closed until the measurable drop in light intensity was

observed. This occurred at ~20 mm diameter; given the focal length of 38.1 mm this gives an effective NA of 0.25.

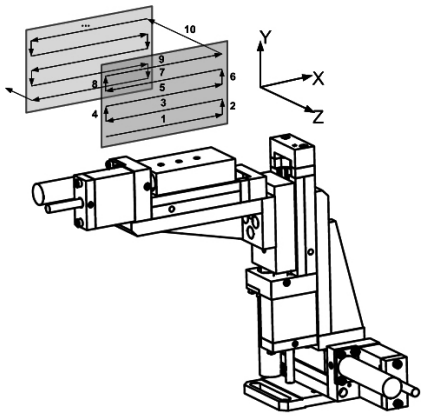

Figure 3. CMIR-TI scanning technique. The numbers represent the sequence of movement of the xyz stages.

The frequency of the chopper was set to 1.6 kHz to achieve stable averaging of 48 samples per data point with the lock-in integration time set to 30 ms according to the Equation 2. Due to the low speed of the stages, finding the minimum value for lock-in integration time $T_{lock\text{-}in}$ and the maximum value for chopping frequency $f_{chopper}$ was not critical. The number of samples N acquired by the lock-in amplifier per data point is:

$$N = f_{chopper} \cdot T_{lockin} \quad N = f_{chopper} \cdot T_{lockin} . \qquad \text{(Equation 2)}$$

The value of 48 samples per data point indicates that the lock-in amplifier acquires 48 values of the signal for one data point plotted in the generated image. This increases the SNR value during the measurement [34]. The optimized settings are discussed in detail later in section 3.2.

3.0. Experimental measurements

3.1. Evaluation of resolution and scanning speed

To quantify the quality of the images acquired with the CMIR-TI and MIR-TI techniques, and their potential limitations, the resolution of both systems was measured to establish the smallest feature size which can be detected. The USAF standard resolution testing target was placed in the CMIR-TI system in place of the Y-TZP sample. The USAF testing target pattern consists of three dark lines against a light, transparent background (positive testing target). The pattern occurs in pairs in horizontal and vertical orientation of three lines. Each pair of horizontal and vertical line pattern creates one element. These elements are arranged in groups of six element pairs each [35]. Each target group has smaller bars compared to the previous group so that the

resolution of the investigated imaging system can be determined. The higher the group number the smaller are the bars.

Due to the limited optical transmittance in the mid-infrared of a standard, off-the-shelf, USAF testing target on soda-lime glass, an infrared transmitting testing target was prepared based on USAF 1951 T-20 target (according to the MIL-STD-150A standard). A 1 mm thick Calcium Fluoride (CaF_2) glass window was chosen because of its high optical transmittance in the mid-infrared wavelength region. The glass was coated with Aluminium (170 nm thick) using a thermal evaporation technique. The target bars were laser machined by ablating the aluminium layer using a 343 nm wavelength Trumph TruMicro 5050 picosecond laser system. For the purpose of the resolution measurement only groups 2 and 3 of the USAF targets were machined. A picture of the laser machined infrared target on the CaF_2 window is shown in Figure 4. The bar dimensions of the machined infrared target differ by 9% from the standardized dimensions, therefore a resolution reading error of 9% has to be taken into account.

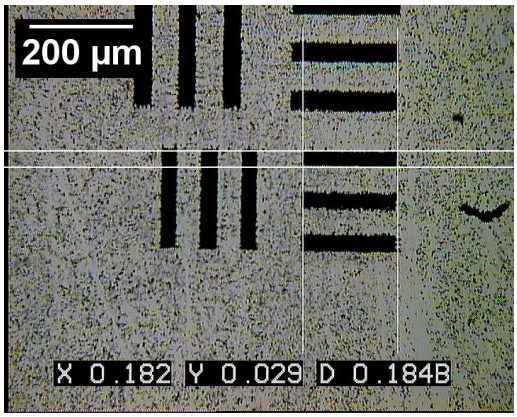

Figure 4. Microscope image of the machined testing target bars. The image presents the sixth element from the third group.

The results for measurements made with the CaF_2 resolution target are presented in Figure 5 (images acquired during 50, 25 and 10 um step scanning) and Figure 6 (MIR-TI technique). The resolution calculated from the images for the MIR-TI system is 39.4 µm (group 3, element 5) and for the CMIR-TI system for 50 µm steps is 49.6 µm (group 3, element 3), for 25 µm and 10 µm steps is 35 µm (group 3, element 6).

a) b) c)

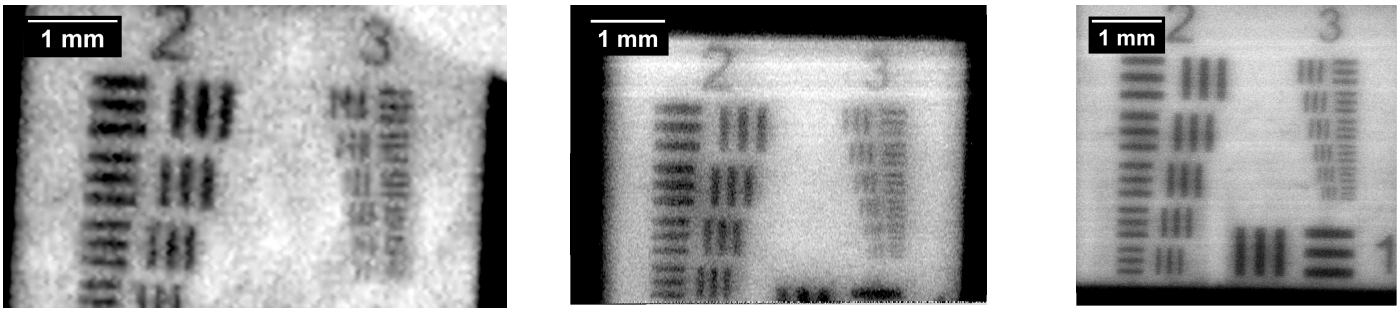

Figure 5. CMIR-TI resolution measurements using the infrared testing target for: a) 50 µm; b) 25 µm; c) 10 µm steps.

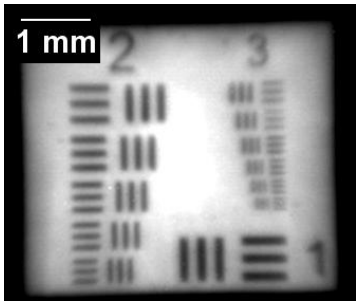

Figure 6. MIR-TI resolution result with the infrared testing target.

The resolution measurements described above were carried out using the broad wavelength range available from the infrared source (1-11 microns). Consequently, for the CMIR-TI technique the wavelength range was limited by the infrared detector which operates with range 2.5 – 9 µm. For the MIR-TI technique the spectral limitation was the infrared source at the long wavelength end (11 µm cut-off) and the Germanium camera lens (2 µm cut-off) at the short wavelength end. Such a wide spectral range introduces additional noise due to chromatic aberrations. To reduce the effects of this aberration a band-pass infrared filter was introduced into the optical path to limit the measurement of resolution to a range between 3 and 6 µm. The resolution measurement with the infra-red band pass filter more accurately represents the resolution when testing Y-TZP samples as the Y-TZP itself would act like a filter due to its limited transmission window in the mid-IR (Figure 7).

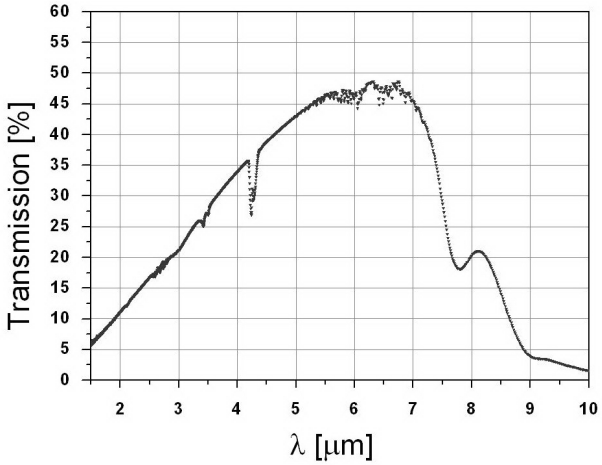

Figure 7. Optical transmittance of 300 μm thick Y-TZP measured with Fourier Transform Infrared Spectroscopy (FT-IR).

The resolution measurements were therefore repeated with the band-pass filter and the images obtained are presented in **Error! Reference source not found.**. An improvement in image sharpness especially for the 10 μm step using the CMIR-TI scanning is observed. For 25 and 10 μm steps the resolution is at least 35 μm (group 3 element 6) whereas for 50 μm the resolution achieved is 44 μm (group 3, element 4). It should also be noted that there is an apparent observed improvement in the resolution when comparing Figure 5(c) and **Error! Reference source not found.**(c) i.e. a 10 μm step size compared to a 10 μm step size with the band-pass filter. This improvement was not quantifiable however because the USAF target bars could not be machined effectively below 35 μm (group 4 bars). Manufacturing testing targets with smaller bars could help to discriminate this perceived resolution improvement but unfortunately due to limitations of the laser machining process this was not feasible.

a) b)

c) d)

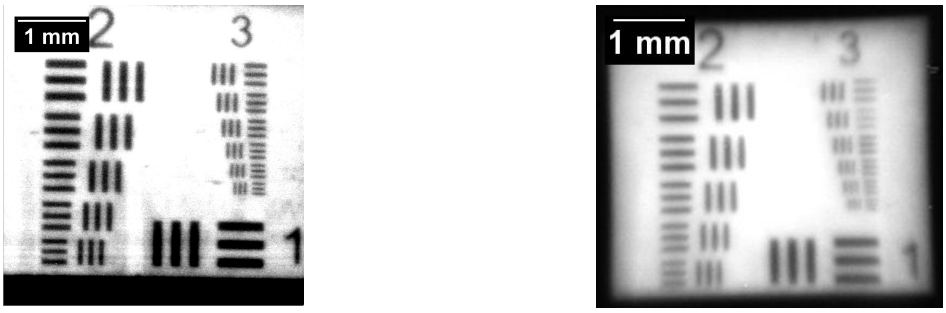

Figure 8. Resolution measurements using the infrared band-pass filter (3 to 6 microns) for: a) 50 µm, b) 25 µm, c) 10 µm CMIR-TI system scanning; d) MIR-TI measurement.

For the MIR-TI system, on the other hand, there is little difference when using an infrared band-pass filter. This is because the normalised optical detectivity of the camera sensor in the mid-infrared is 5 times lower [36]. Poor camera detectivity between 4 and 6 µm negates any resolution improvement with the band-pass filter due to reduced SNR. Consequently any potential effects of reduced chromatic aberrations were not measurable. To add more it is likely that if the USAF target was machined on the surface of the Y-TZP the influence of the narrower wavelength band would be more significant but due to difficulties in machining sharp and smooth edges it was not feasible. The testing target measurement on the other hand presents the ideal case where no scattering is present.

The detectivity, D, of the sensor is the reciprocal of the Noise Equivalent Power (NEP) [37]. NEP is the incident power on the detector generating an output signal equal to the root mean square (RMS) output noise, i.e. the signal level that produces a SNR of 1. NEP is proportional to the square root of the detector signal that is proportional to the detector area A_d. Normalised detectivity D* , which depends on detector area, A_d, was used to compare the infrared camera and Vigo sensors and is defined by Equation 3[37]:

$$D^* = \frac{(A_d \Delta f)^{1/2}}{NEP}. \qquad \text{(Equation 3)}$$

where Δf is effective noise bandwidth. The advantage of D* is the fact that it allows for comparison of detectors that have different active regions. The detector used in the CMIR-TI has a higher detectivity compared to that of the camera sensor used in the MIR-TI and consequently this leads to a higher SNR and therefore an improved resolution.

3.2. Crack detection in laser machined samples

The CMIR-TI technique was employed to investigate a series of laser machined samples. Figure 1 presents the first sample tested. A series of holes were drilled using a Lumonics JK705 Nd:YAG millisecond pulsed laser system in 2.7 mm thick sample. Due to the high thermal input of the millisecond laser pulses and low thermal conductivity of Y-TZP [38] cracking may appear leading to component failure. In this instance several cracks were located. The impact of the varying scanning step sizes of the CMIR-TI system on the quality of acquired images using sample 1 is presented in

Figure 10. These images were acquired with CMIR-TI system positioned 1.5 mm from the sample surface from the detector side. The improvement in image quality with reduced the step size is clear, hence the remaining samples presented in this paper were scanned using a 10 µm step size in x and in y axis.

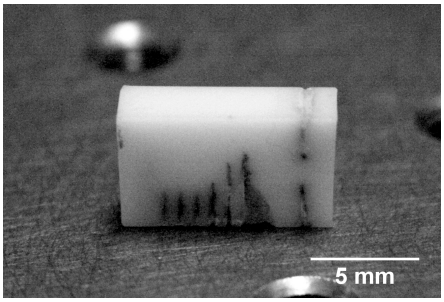

Figure 9. Sample 1 machined with a millisecond laser system.

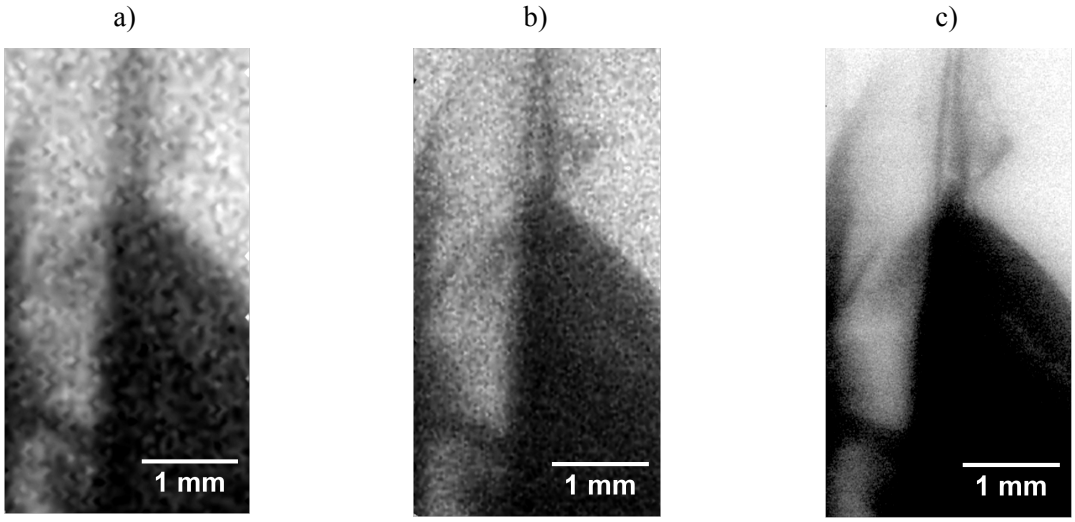

Figure 10. The comparison of the image sharpness as a function of CMIR-TI scanning step sizes: a) 50 µm; b) 25 µm; c) 10 µm steps in x and y axis. The images acquired at 1.5 mm sample depth from the detector side.

These measurements revealed the presence of cracks which had been identified on the surface, and within the bulk from the infrared source side (Figure 11). Cracks 1 and 4 were identified as being surface cracks. Cracks 2 and 3 were not found on the surface of the sample. The depths of the cracks were calculated from the acquired images (based on the scanning position) and the sample was sectioned at this depth to verify the presence of the flaws. Crack 2 was 1.5 mm below the surface and crack 3 was 300 µm below the surface, as viewed from the detector side. A Scanning Electron Microscope (SEM) and Environmental Scanning Microscope (ESEM) were used to measure the size of the cracks detected (Figure 12). The same sample was tested with the previously reported MIR-TI technique [33] which shows good agreement with the result achieved using CMIR-TI technique.

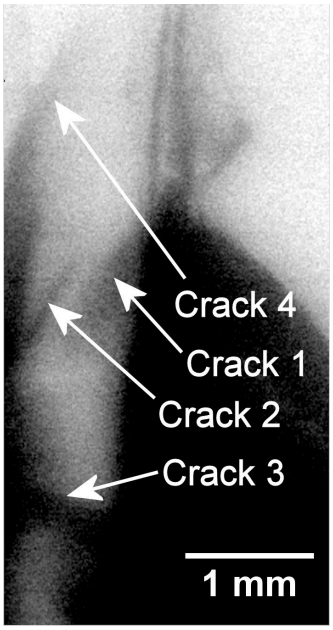

Figure 11. Cracks detected in sample 1.

a)

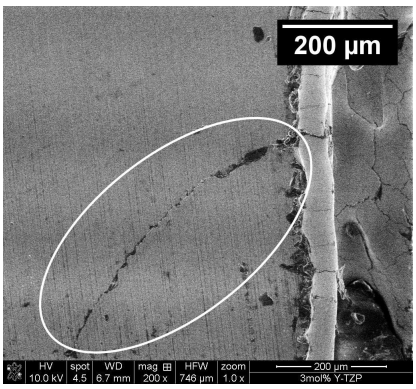

b)

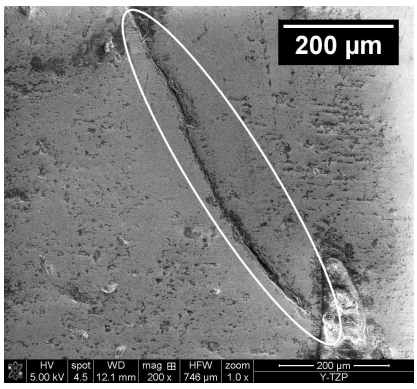

c)

d)

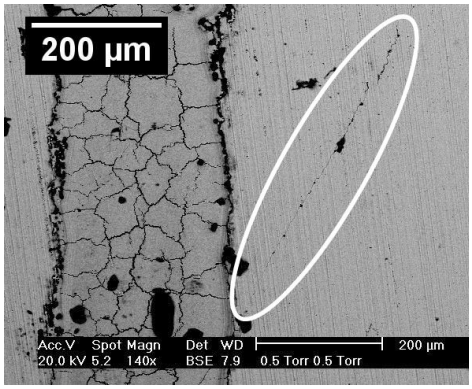

Figure 12. SEM images of the crack 1 (a), crack 2 (b), microscope image of crack 3 (c) and ESEM image of crack 4 (d) detected in Y-TZP sample. Cracks 1 (a) and 4 (d) are the surface cracks, whereas cracks 2 (b) and 3 (c) were located in the bulk of the sample after sectioning.

Figure 13 presents another machined Y-TZP specimen (3.76 mm thick) tested with the CMIR-TI technique. This sample was machined using a fibre laser [39]. The fibre laser machining process employs a controlled crack propagation technique to cut through the sections of Y-TZP material, which substantially increases the thicknesses of Y-TZP components which can be machined in a single process [39]. The CMIR-TI inspection detected a high number of cracks within the bulk material at 2.1 mm sample depth (Figure 14). The cracks were present between the laser drilled holes indicating that a controlled crack propagation process was initiated. The sample was then sectioned to validate the presence of the cracks. Figure 15 presents the SEM images of some of the cracks detected with CMIR-TI technique.

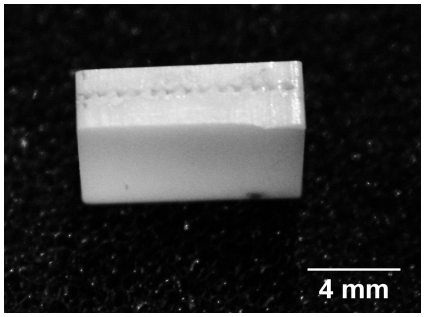

Figure 13. Sample 2 – a 3.76 mm thick fibre laser machined sample.

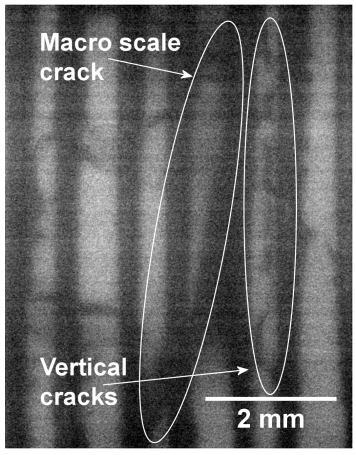

Figure 14. CMIR-TI result of sample 1 from Figure 13. The image taken 2.1 mm from the sample surface from the detector side

a) b)

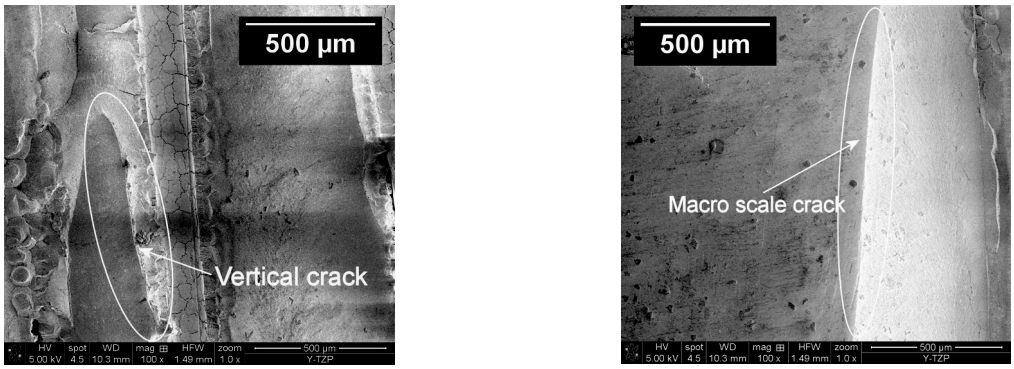

Figure 15. SEM images of the cracks detected. Figure a) presents the vertical edge of crack and figure b) shows the edge of the crack which propagated through the whole sample.

To compare the results between the MIR-TI technique (reported previously by this group [33]) and the CMIR-TI technique each sample investigated was also tested using the MIR-TI system. This therefore allows comparison of the systems and an evaluation of the performance and suitability for detection of cracks within the bulk of zirconia ceramics. The MIR-TI results of the measured samples (samples 1 and 2) are illustrated in Figure 16. The CMIR-TI and MIR-TI images are comparable, although the images with the confocal system provide an enhanced contrast and detection of a higher number of the micro-scale features for thin samples.

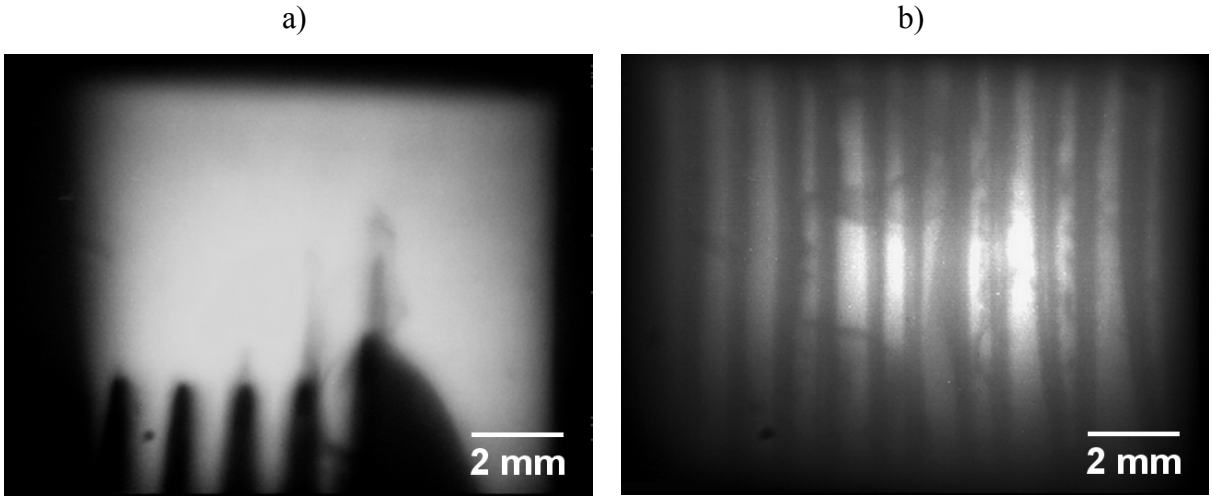

Figure 16. MIR-TI images of: a) sample 1 (1.5 mm away from the surface); b) sample 2 (2 mm away from the surface).

The scanning speed of the CMIR-TI technique is significantly limited by the velocity of the motorized stages and the signal chopping frequency. The maximum stage velocity is 160 µm/s, whereas the chopping frequency is limited to 4 kHz for these experiments due to a combination of chopping disc aperture spacing and the motor speed. Therefore to estimate the viability of the CMIR-TI technique for industrial applications, where faster scanning is desirable, the calculations of the scanning speeds

based on currently available equipment were carried out. Faster motion stages such as the Aerotech ABL1000 air bearing stages (300 mm/s) are available as are faster chopping frequencies with the Scitec 300D200 (40 kHz) chopping disc hence these parameters were used to estimate the potential improvement in scanning times.

During the measurements presented in this paper the number of samples N was set to 48 to maximize the SNR. In order to calculate the maximum feasible scanning speed of the CMIR-TI system a series of measurements was performed that indicated that even with N = 8 an acceptable acquired signal quality was achieved, thus speeding up the process. Based on the 40 kHz chopping frequency and N = 8 the lock-in integration time $T_{lock\text{-}in}$ = 200 μs was calculated (Equation 2). For these values the required speed for the motorized stages are presented in Table 1. These speeds are within the specification of several currently available motorized stage models. For a CMIR-TI system using an Aerotech ABL1000 air bearing stage and a Scitec 300D200 chopper the scanning times of 5 x 5 mm area would require 2 s with 50 μm step scanning, 8 s with 25 μm steps and 50 s with 10 μm steps, thus significantly reducing the component inspection time and demonstrating its feasibility for integration as a quality control measure.

Table 1. The required motorized stage velocity for the chopping frequency $f_{chopper}$ = 40 kHz and the lock-in integration time $T_{lock\text{-}in}$ = 200 μs.

Scanning step size	**Stages velocity**
10 μm	50 mm/s
25 μm	125 mm/s
50 μm	250 mm/s

4.0. Discussion

This non-destructive optical inspection technique of multicrystalline Y-TZP ceramics is a significant challenge due to optical scattering [20, 40]. Strong light scattering, especially in the visible wavelength region, occurs due to the grain size of the Y-TZP material (Figure 17) which is comparable with visible wavelengths [33]. The improved optical transmission in the mid-infrared arises as the wavelength of light becomes larger in comparison with the grain size reducing scattering. Consequently, a mid-infrared based technique allows for crack inspection of thick Y-TZP components.

It should be noted though, that the samples presented include only the inspection of the smooth surface parts. Any deviation from the smooth surface finish will reduce the contrast of the produced images due to increased light scattering, across the whole optical spectrum [41, 42].

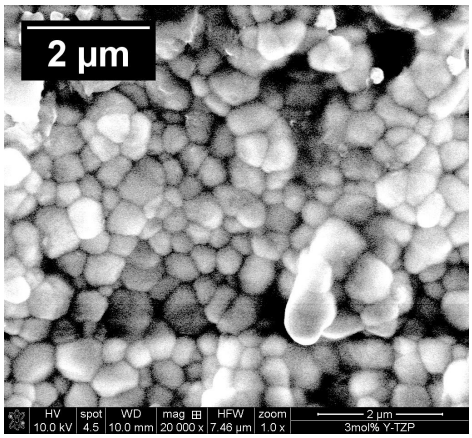

Figure 17. SEM image of the Y-TZP grains showing an average grain size of approximately 0.5 µm. This is comparable to visible wavelengths causing significant scattering in this region but results in reduced scattering for the mid-infrared wavelengths in the 6 µm region.

Both laser machining and conventional mechanical grinding of ceramics introduce significant, and localized, heat and stress into the material which often leads to the generation of cracks which have serious detrimental effects on the mechanical properties. The micro scale cracks can be detected due to the air gap giving the refractive index discontinuity. This leads to reflection and refraction providing darker regions in the neighbourhood of the crack (Figure 10, Figure 14) [33].

The CMIR-TI technique presented in this paper offers improved resolution (compared to the previously reported MIR-TI technique) clearly demonstrating the advantages of using a confocal pinhole configuration. Additionally, by reducing the step size during scanning it is possible to detect fine cracks. It should be noted that a confocal pinhole configuration could also be performed with the camera used in the MIR-TI system with similar gains in resolution expected if the NA of the imaging system was reduced to the NA value for the CMIR-TI technique. Unfortunately the low optical power of the infrared source and lower detectivity of the camera sensor compared to the Vigo detector make such setup not feasible.

The increased imaging resolution and contrast of the CMIR-TI images compared to those generated by MIR-TI technique is achieved by the reduced step size during CMIR-TI scanning. The increased number of data points allows for an enhanced reconstruction of the scanned area even though the pinhole size is larger compared to the step size. Furthermore, the high detectivity of the Vigo detector considerably improves the SNR of the CMIR-TI system. Conversely, the small pinhole size introduces a SNR challenge due to a lower signal level incident the infrared detector. Consequently, further reduction of the pinhole size for the CMIR-TI system was not possible with the available broadband thermal source.

An additional improvement of the image quality using CMIR-TI technique is possible with the reduction of the pinhole diameter given the improvement in image resolution with reduced step size shown in Figure 10 but this would have to be accompanied by an introduction of more powerful or

coherent infrared source. Such a coherent infrared source with a much narrower wavelength emission spectra would also reduce chromatic aberration problems. However, a coherent source would give rise to speckle.

To quantify the smallest features which can be resolved by both infrared techniques the resolution capabilities of the CMIR-TI and MIR-TI systems have been investigated. For the purpose of the experiment an infrared transparent USAF 1951 testing target was fabricated. As anticipated an increased number of data points during 25 and 10 μm scanning resulted in an improved imaging resolution. Further enhancement of the resolution was achieved for the CMIR-TI technique when using an infrared band-pass filter in the optical path (**Error! Reference source not found.**) compared to the measurement without the filter. By restricting the spectral range (3 to 6 microns) the diffraction effects of the pinhole and the chromatic aberrations are reduced [43]. This enhancement was not seen in the MIR-TI system, because of the reduced detectivity of the camera sensor in the mid-infrared region which counteracts any potential gains from reduced chromatic aberration.

It is clear that this investigation has shown that both CMIR-TI and MIR-TI techniques are capable of detecting defects in the bulk material. The limit of detection for micro scale features was determined for the CMIR-TI system by performing a series of measurements on samples of various thickness. With a thickness of up to 3.5 mm the cracks can be detected provided that they have a size above the resolution limit in at least two dimensions. For example, crack 2 detected in the bulk volume of Sample 1 (Figure 11) was detected even though it was only a few microns wide. After the sample was sectioned the depth of the crack was estimated to be approximately 240 μm which is well above the resolution limits of CMIR-TI system. For a sample thickness greater than 3.5 mm the signal reaching the detector becomes comparable to the noise level, and so the detection of flaws becomes a challenge.

The results obtained for the Y-TZP samples show a marked improvement with reduced step size (Figure 10). For example there is ×25 more data acquired for Figure 10(c) compared to Figure 10(a) due to the reduced step size which improves the SNR. Furthermore the quality of Figure 10(a) could potentially be improved if 25 images were averaged together. When testing thicker Y-TZP samples the image becomes increasingly blurred due to a reduction in the signal. The blurring effect is again suppressed by using a smaller step size which sharpens the image due to an improved SNR. Hence a 10 μm step scanning improves image quality and there is a noticeable resolution difference between 50 μm, 25 μm and 10 μm step scanning.

The presented CMIR-TI technique although considerably slow can be improved when a more sophisticated setup is used. The scenario presented verify that the scanning times can be significantly improved, although the challenge of providing high chopping frequencies above 40 kHz when using

high speed stages still exists. Nevertheless significantly reduced inspection times are promising for the industrial application.

5.0. Conclusions

We have presented a viable technique for the detection of cracks within the bulk of Y-TZP ceramics of thickness up to 3.5 mm. The CMIR-TI results are improved over the previously reported MIR-TI results [33, 43] for thinner Y-TZP components by employing a confocal pinhole configuration. The CMIR-TI technique could potentially be applied during inspection of dental parts (which are often caps or veneers much thinner than 3.5 mm) where detecting flaws in final parts is vital to ensure reliability in service. Additionally, this technique could be applied more generally to processing of Y-TZP components providing detailed information about material condition after either a mechanical or laser machining process. Currently the only way of performing this vital non-destructive testing on Y-TZP parts is by human inspection which is expensive and subjective depending on the person carrying out the measurement.

Although the time required for the CMIR-TI image acquisition is significantly greater than MIR-TI image acquisition, this can be greatly enhanced using an optimised chopper and motion stage arrangement. It has been demonstrated that with these improved components scanning times of practical parts (5 x 5 mm) can be less than 1 minute making CMIR-TI viable for integration into a semi-automated production line.

Acknowledgements

The authors wish to thank the FIC-SEM Heriot Watt University facility for the access to Scanning Electron Microscope apparatus. Financial support provided by Engineering and Physical Sciences Research Council (EPSRC) and Renishaw plc is also acknowledged.

References

1. Vallet-Regi M, Ceramics for medical applications, Journal of the Chemical Society, Dalton Transactions, 2001: 97-108.
2. Koutayas SOV, Thaleia; Pelekanos, Stavros; Koidis, Petros; Strub, Jorg Rudolf, Zirconia in dentistry: part 2. Evidence-based clinical breakthrough., The European Journal of Esthetic Dentistry, 2009; 4(4): 348-80.
3. Özkurt Z, Kazazoğlu E, Clinical Success of Zirconia in Dental Applications, Journal of Prosthodontics, 2010; 19(1): 64-8.
4. Miller RA, Current status of thermal barrier coatings -- An overview, Surface and Coatings Technology, 1987; 30(1): 1-11.
5. Cao XQ, Vassen R, Stoever D, Ceramic materials for thermal barrier coatings, Journal of the European Ceramic Society, 2004; 24(1): 1-10.
6. Vleugels J, Fabrication, wear and performance of ceramic cutting tools, Ind Ceram, 2008 Sep; 28(2): 145-52.

7. Birkby I, Stevens R. Applications of zirconia ceramics. Advanced Ceramic Materials. Clausthal Zellerfe: Trans Tech Publications; 1996. p. 527-51.
8. Green D.J HR, Swain M.V. Transformation toughening of ceramics. CRC Press;. 1988.
9. Laurence Ruiz MJR, Effect of Heat Treatment on Grain Size, Phase Assemblage, and Mechanical Properties of 3 mol% Y-TZP, J Am Ceram Soc, 1996; 79(9): 2331-40.
10. Denry I, Kelly JR, State of the art of zirconia for dental applications, Dental Materials, 2008 Mar; 24(3): 299-307.
11. Weigl P, Kasenbacher A, Werelius K. Dental applications. Femtosecond Technology for Technical and Medical Applications. Berlin: Springer-Verlag Berlin; 2004. p. 167-85.
12. Chevalier J, Gremillard L, Ceramics for medical applications: A picture for the next 20 years, Journal of the European Ceramic Society, 2009; 29(7): 1245-55.
13. Kosmac T, Oblak C, Marion L, The effects of dental grinding and sandblasting on ageing and fatigue behavior of dental zirconia (Y-TZP) ceramics, Journal of the European Ceramic Society, 2008; 28(5): 1085-90.
14. Novikov NV, Rozenberg OA, Mamalis AG, Sokhan SV, Finish diamond machining of ceramic femoral heads, Int J Adv Manuf Technol, 2005 Feb; 25(3-4): 244-7.
15. Dear FC, Shephard JD, Wang X, Jones JDC, Hand DP, Pulsed laser micromachining of yttria-stabilized zirconia dental ceramic for manufacturing, International Journal of Applied Ceramic Technology, 2008; 5(2): 188-97.
16. Parry JP, Shephard JD, Dear FC, Jones N, Weston N, Hand DP, Nanosecond-laser postprocessing of millisecond-laser-machined zirconia (Y-TZP) surfaces, International Journal of Applied Ceramic Technology, 2008; 5(3): 249-57.
17. Wang X, Shephard JD, Dear FC, Hand DP, Optimized nanosecond pulsed laser micromachining of Y-TZP ceramics, J Am Ceram Soc, 2008 Feb; 91(2): 391-7.
18. Parry JP, Shephard JD, Hand DP, Moorhouse C, Jones N, Weston N, Laser Micromachining of Zirconia (Y-TZP) Ceramics in the Picosecond Regime and the Impact on Material Strength, International Journal of Applied Ceramic Technology, 2009: no-no.
19. Luthardt RG, Holzhuter MS, Rudolph H, Herold V, Walter MH, CAD/CAM-machining effects on Y-TZP zirconia, Dental Materials, 2004; 20(7): 655-62.
20. Eldridge JI, Spuckler CM, Markham JR, Determination of Scattering and Absorption Coefficients for Plasma-Sprayed Yttria-Stabilized Zirconia Thermal Barrier Coatings at Elevated Temperatures, J Am Ceram Soc, 2009 Oct; 92(10): 2276-85.
21. Singh KJ, Matsuda Y, Hattori K, Nakano H, Nagai S, Non-contact sound velocities and attenuation measurements of several ceramics at elevated temperatures, Ultrasonics, 2003; 41(1): 9-14.
22. Andrews D, Taylor J, Quality control of thermal barrier coatings using acoustic emission, Journal of Thermal Spray Technology, 2000; 9(2): 181-90.
23. Serra E, Tucci A, Esposito L, Piconi C, Volumetric determination of the wear of ceramics for hip joints, Biomaterials, 2002; 23(4): 1131-7.
24. Corfield V, Khan I, Scott R. Hydrothermal Stability of Ceramic Femoral Heads. Bioceramics and Alternative Bearings in Joint Arthroplasty2007. p. 59-64.
25. Newaz G, Chen X, Progressive damage assessment in thermal barrier coatings using thermal wave imaging technique, Surface and Coatings Technology, 2005; 190(1): 7-14.
26. Ferber MK, Wereszczak AA, Lance M, Haynes JA, Antelo MA, Application of infrared imaging to the study of controlled failure of thermal barrier coatings, J Mater Sci, 2000 Jun; 35(11): 2643-51.
27. Eldridge JI, Spuckler CM, Martin RE, Monitoring delamination progression in thermal barrier coatings by mid-infrared reflectance imaging, International Journal of Applied Ceramic Technology, 2006; 3(2): 94-104.
28. Bashkansky M, Duncan MD, Kahn M, Lewis Iii D, Reintjes J, Subsurface defect detection in ceramics by high-speed high-resolution optical coherent tomography, Opt Lett, 1997; 22(1): 61-3.
29. Bashkansky M, Duncan MD, Kahn M, Reintjes J, Battle PR, editors. Subsurface defect detection in ceramic materials using an optical gated scatter reflectometer. Lasers and Electro-Optics, 1996 CLEO '96, Summaries of papers presented at the Conference on; 1996 2-7 June 1996.
30. Bashkansky M, Duncan MD, Reintjes JF, editors. Optical gating techniques for material inspection. Sensors and Controls for Advanced Manufacturing; 1998; Pittsburgh, PA, USA: SPIE.

31. Veilleux J, Moreau C, Lévesque D, Dufour M, Boulos M, Optical Coherence Tomography for the Inspection of Plasma-Sprayed Ceramic Coatings, Journal of Thermal Spray Technology, 2007; 16(3): 435-43.
32. Visher RJE, W. A. ; Shields, M. D.; Feuerstein, A. , editor. Laser-Based Inspection of Thermal Barrier Coatings. Surface Engineering—Proceedings of 3rd International Surface Engineering Congress; 2004; Orlando, FL.
33. Matysiak M, Parry JP, Crowder JG, Hand DP, Shephard JD, Jones N, Jonas K, Weston N, Development of Optical Techniques for Noncontact Inspection of Y–TZP Parts, International Journal of Applied Ceramic Technology, 2011; 8(1): 140-51.
34. Busch KW, Busch MA, Ythier RM, Kuehn AJ, Design Parameters for an Optimized Flame/Furnace Infrared Emission (FIRE) Radiometer, Appl Spectrosc, 1993; 47(12): 2072-80.
35. Goncalves DP, Griffith DJ, Estimating uncertainty in resolution tests, Opt Eng, 2006 May; 45(5).
36. Website www.electrophysics.com.
37. Piotrowski J, Rogalski A. High-Operating-Temperature Infrared Photodetectors: SPIE; 2007.
38. Willmann G, Früh HJ, Pfaff HG, Wear characteristics of sliding pairs of zirconia (Y-TZP) for hip endoprostheses, Biomaterials, 1996; 17(22): 2157-62.
39. Parry J, Ahmed R, Dear F, Shephard J, Schmidt M, Li L, Hand D, A Fiber-Laser Process for Cutting Thick Yttria-Stabilized Zirconia: Application and Modeling, International Journal of Applied Ceramic Technology, 2009: no-no.
40. Reicher D, Jungling K, Influence of crystal structure on the light scatter of zirconium oxide films, Appl Opt, 1997; 36(7): 1626-37.
41. Bohren CF, Huffmann DR. Absorption and Scattering of Light by Small Particles. New York: Wiley; 1998.
42. Hulst HCvd. Light Scattering by Small Particles: Dover Publications; 1981.
43. Durant S, Calvo-Perez O, Vukadinovic N, Greffet J-J, Light scattering by a random distribution of particles embedded in absorbing media: full-wave Monte Carlo solutions of the extinction coefficient, J Opt Soc Am A, 2007; 24(9): 2953-62.